nature materials

Article

https://doi.org/10.1038/s41563-025-02274-y

Homoepitaxial growth of large-area rhombohedral-stacked MoS_2

Received: 29 April 2024

Accepted: 23 May 2025

Published online: 09 July 2025

Check for updates

Lei Liu[1,2,13], Taotao Li[2,3,4,13], Xiaoshu Gong[2,5,13], Hengdi Wen[1,13], Liqi Zhou[6], Mingwei Feng[3], Haotian Zhang[3], Ningmu Zou[3,4], Shengqiang Wu[2], Yuhao Li[1], Shitong Zhu[1], Fulin Zhuo[1], Xilu Zou[1], Zehua Hu[1], Zhiyuan Ding[7], Susu Fang[8], Weigao Xu[8], Xingang Hou[9], Kai Zhang[9], Gen Long[2], Lei Tang[10], Yucheng Jiang[11], Zhihao Yu[12], Liang Ma[2,5], Jinlan Wang[2,5] & Xinran Wang[1,2,3,4] ✉

Interlayer stacking is an important degree of freedom to tune the properties of two-dimensional materials and offers enormous opportunities for designing functional devices. As a classic example, rhombohedral-stacked (3R) two-dimensional materials exhibit ferroelectricity and optical nonlinearity that are non-existent in naturally abundant hexagonal-stacked (2H) counterparts. However, the ability to grow stacking-controlled large-area films remains challenging due to the thermodynamic competition of different polytypes. Here we report the chemical vapour deposition growth of two-inch wafer-scale 3R-MoS_2 films with high phase purity by homoepitaxy on top of a crystalline monolayer MoS_2. A defect-promoted nucleation mechanism was proposed, in which Mo-substituted sulfur vacancy is identified as one of the possible defects promoting 3R stacking. We fabricate ferroelectric semiconductor field-effect transistors with 3R-MoS_2 channels and demonstrate non-volatile memory characteristics. The control of interlayer stacking is an essential step towards the large-scale production of two-dimensional materials for multifunctional integration.

Future electronics beyond Moore's path require multifunctional integration, where materials and devices with different functionalities, such as memory, sensor and optoelectronics, are all integrated monolithically[1]. Two-dimensional (2D) transition metal dichalcogenides (TMDs) are important material candidates for transistor scaling and monolithic three-dimensional integration[2,3]. To achieve this goal, we need to engineer materials with the desired properties, and interlayer stacking is one of the most important tuning parameters for 2D materials. In fact, many exotic properties are observed in artificially stacked multilayer 2D materials that are non-existent in naturally abundant counterparts, such as ferroelectricity[4–8], superconductivity[9], topological insulator[10] and valleytronics[11,12]. However, early proof-of-concept demonstrations rely on either mechanically stacked moiré structures[5] or preselected flakes from stacking uncontrolled chemical vapour deposition (CVD) growth[13,14]. The lack of interlayer stacking control in CVD thus far poses substantial challenges in large-scale device integration.

Many semiconducting TMDs (such as MoS_2 and WSe_2) have two thermodynamically stable polytypes, namely, 2H and 3R. The 2H (3R) phase has a unit cell composed of bilayers (trilayers) with an interlayer twist angle of 180° (0°). In the 3R phase, each layer in the unit cell slides $\frac{\sqrt{3}}{3}a$ along the armchair direction (where a is the lattice constant), giving rise to inversion symmetry breaking. Recent works show the promise of 3R-TMDs in nonlinear optics[15], ferroelectrics[8] and bulk photovoltaics[16] owing to their non-centrosymmetric structure. Currently, the main preparation method for 3R-TMDs relies on mechanical exfoliation from a bulk rhombohedral crystal[11,17,18], which suffers from a small flake size and low productivity. On the other hand, CVD is a more promising technique to produce large-area films[19,20], but has limited success so far in growing a stacking-controlled 3R phase[21–23].

A full list of affiliations appears at the end of the paper. ✉e-mail: xrwang@nju.edu.cn

https://doi.org/10.1038/s41563-025-02274-y

Importantly, the lack of mechanistic insights to preferentially grow 3R stackings over other competing phases (especially the most thermodynamically stable and abundant phase is 2H) prevents the large-area growth of 3R-stacked TMDs[24–26].

In this work, we grow 3R-MoS_2 films with high phase purity (~99.86%) on a two-inch sapphire substrate by CVD. The growth is based on homoepitaxy, where the first single-crystalline MoS_2 layer serves as the template for the nucleation of upper layers in a Mo-rich environment. Combining extensive experiments with density functional theory (DFT) calculations, we propose a defect nucleation mechanism in which a Mo-substituted sulfur vacancy (Mo_S) is identified as the most likely nucleation centre for 3R-MoS_2. Such a hypothesis is corroborated by the existence of Mo_S within an early nucleation cluster captured by scanning transmission electron microscopy (STEM). We further confirm the presence of ferroelectricity in the 3R-MoS_2 films and fabricate ferroelectric semiconductor field-effect transistors (FeS-FETs) showing >10-year retention time and multibit storage capacity at room temperature.

Homoepitaxial growth of large-area 3R-MoS_2

The CVD growth was carried out in a custom tube furnace (Supplementary Fig. 1) by a two-step process, where a continuous single-crystal monolayer was formed in the first step on *c*-plane sapphire substrates with a miscut angle of 1° towards the *a* axis (*c*/*a* – 1°; ref. 27) and the upper layers were grown in the second step (Methods). During the second step, we increased the Mo concentration in situ by elevating the source temperature without breaking the vacuum. Control experiments that expose the first MoS_2 layer to ambient conditions or oxygen after the first step result in mixed 3R and 2H phases, which will be discussed later. Figure 1a shows two-inch wafers after the first and second growth steps, respectively, showing good wafer-scale uniformity. The monolayer MoS_2 wafer demonstrates single-crystalline characteristics as evidenced by second-harmonic generation (SHG) mapping and low-energy electron diffraction (LEED; Supplementary Fig. 2). Figure 1c presents an optical microscopy (OM) image of a multilayer 3R-MoS_2 film, in which the first layer is complete and the triangular domains are mostly 2–5 layers. Remarkably, the upper layers exhibit unidirectional alignment regardless of the number of layers. The 3R stacking is confirmed by cross-sectional high-angle annular dark-field (HAADF) STEM imaging of a multilayer region (Fig. 1b and Supplementary Fig. 3), where each layer retains the same orientation but shifts along the $(10\bar{1}0)$ direction by $\frac{\sqrt{3}}{3}a = 0.182$ nm. The unit cell contains three layers, and the fourth layer is precisely aligned with the first layer. On the basis of the OM images, we utilize a pixel-level machine learning classification artificial intelligence (AI) model to automatically map out the number of layers and domain orientations (Fig. 1d,e and Supplementary Figs. 4 and 5). For the particular sample shown in Fig. 1c, it comprises 100% monolayer, 98.3% bilayer, 69.8% trilayer, 16.3% quadruple layer, 3.9% pentalayer or more (Fig. 1f). The number of layers obtained by the AI model is further corroborated by Raman spectroscopy, where the separation of the E_{2g} and A_{1g} peaks is 19.2 cm^{-1} for monolayer and gradually increases to 24.5 cm^{-1} for the quadruple layer (Fig. 1g). The phase purity of 3R stacking is calculated to be 99.86% from more than 4,000 domains across the entire wafer (the anti-parallel 2H domains are identified by the pink colour in Supplementary Fig. 5). We also perform LEED with a spot size of ~1 mm (Fig. 1h). The LEED pattern shows three diffraction spots, revealing the non-centrosymmetric 3R stacking over a large area.

Spectroscopic and structural characterizations of 3R-MoS_2

Next, we perform systematic spectroscopic and structural investigations of interlayer stacking. Figure 2a shows an OM image of continuous monolayer MoS_2 with unidirectional bilayer domains. The corresponding photoluminescence (PL) image (Fig. 2b) distinguishes the dark bilayer regions from the bright monolayer regions due to the direct-to-indirect bandgap transition. The atomic force microscopy (AFM) image shows the clean surface of the as-grown MoS_2 (Fig. 2c). SHG offers a direct spectroscopic method for interlayer stacking. Due to the non-centrosymmetric structure of 3R-MoS_2, the SHG intensity shows a quadratic dependence on the number of layers (Fig. 2d,e). By contrast, the 2H stacked bilayer shows negligible SHG signals due to the centrosymmetric structure (Fig. 2d and Supplementary Fig. 6). Raman and SHG mappings further reveal the uniformity of 3R stacking within and across different domains (Supplementary Fig. 7).

Ultralow-frequency (ULF) Raman spectroscopy is another probe to identify the stacking order as the ULF vibration modes arise from interlayer interactions[28]. *N*-layer MoS_2 possesses $N - 1$ interlayer shear vibrational modes (S modes) and $N - 1$ breathing vibrational modes (B modes)[29]. The ULF Raman spectra of bilayer 3R-MoS_2 and 2H-MoS_2 are shown in Fig. 2f. In the 3R phase, the peaks at 21.3 cm^{-1} and 38.7 cm^{-1} are attributed to the interlayer shear mode (S_1) and breathing mode (B_1), respectively[28]. In the 2H phase, the S_1 mode shows stronger intensity, and the B_1 mode is blueshifted to 40.7 cm^{-1}, consistent with a stronger interlayer coupling. Furthermore, the redshift in the S_{N-1} mode and B_{N-1} mode with the number of layers is observed in the 3R configuration (Supplementary Fig. 7c), which is consistent with the theoretical calculations based on the linear chain model[28].

The 3R stacking is further revealed at the atomic scale by HAADF-STEM (Fig. 3). Figure 3a,b reveals the atomically sharp monolayer/bilayer and bilayer/trilayer interfaces. Figure 3c–e presents the experimental and simulated HAADF-STEM images of mono-, bi- and trilayer 3R-MoS_2. For monolayer MoS_2, the hexagonal rings, consisting of alternating Mo and S_2 columns, exhibit a clear intensity contrast (Fig. 3c,f). For bilayer MoS_2, the HAADF-STEM image reveals an interlayer sliding by $\frac{\sqrt{3}}{3}a$ along the armchair direction, forming three distinct intensities corresponding to S_2, Mo and Mo + S_2 (Fig. 3d,f). For trilayer MoS_2, further sliding of the third layer results in Mo + S_2 in all the atomic columns, showing very subtle differences depending on which layer the S_2 and Mo atoms reside (Fig. 3e,f). In all cases, simulations based on the 3R-MoS_2 structure quantitatively reproduce the experimental data. We further examine the atomic structure at the domain edges and observe that the transition is atomically sharp (Fig. 3f and Supplementary Fig. 8). These results indicate that the commensurate 3R stacking is already established at the growth front.

Thickness control is another critical aspect of 3R-MoS_2. This can be achieved by the Ostwald ripening process[30], in which we periodically interrupt the Mo source to prevent the nucleation of thicker MoS_2 on the top layer. A comprehensive set of characterizations, including OM, AFM and Raman spectroscopy, show large-area uniform bilayer 3R-MoS_2 using this process (Supplementary Fig. 9 and the 'Discussion about the growth of uniform bilayer MoS_2' section in the Supplementary Information).

Growth mechanism of 3R-MoS_2

Next, we discuss the growth mechanism of rhombohedral-stacked MoS_2. The selective growth of the 3R-MoS_2 phase necessitates a substantial difference in formation energy between the 2H and 3R phases. However, the energy difference in the bulk form is too small (approximately 1 meV per MoS_2) to account for the selectivity[19]. Like on the sapphire substrate, the most critical factor influencing the MoS_2 orientation is nucleation. Once the nuclei reach a critical size, they become energetically unfavourable to rotate freely. Several nucleation mechanisms have been proposed for TMD, namely, impurity nucleation, edge nucleation and surface nucleation. Impurity nucleation (such as Re, W, Nb, V, Fe and Ti) was reported in the chemical vapour transport growth of 3R-MoS_2 bulk crystals[18,31]. However, it can be ruled out that no metal impurities were introduced during our growth process. Edge nucleation was reported in the epitaxial growth of 2D materials on single-crystal surfaces with atomic steps such as Au and sapphire[27,32–34]. This mechanism can also

https://doi.org/10.1038/s41563-025-02274-y

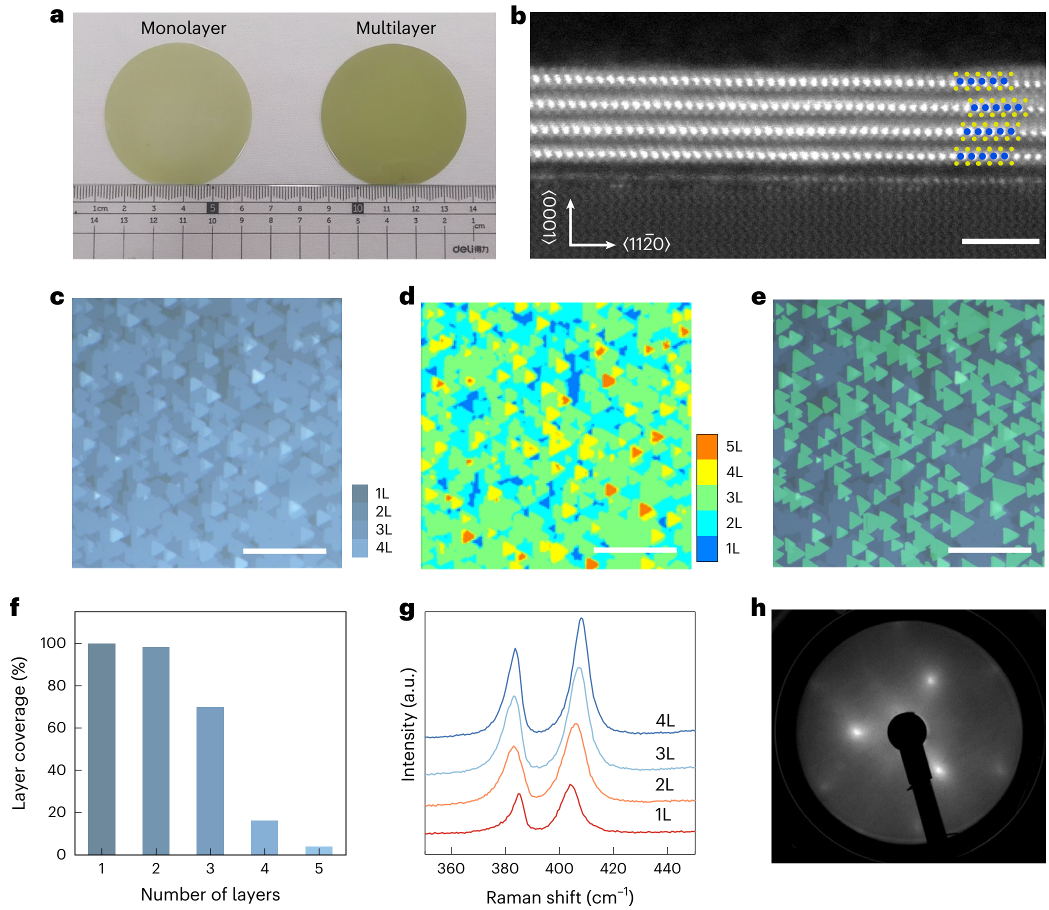

Fig. 1 | Wafer-scale 3R-MoS_2. **a**, Photograph of a monolayer single-crystal MoS_2 film and multilayer 3R-MoS_2 wafers. The optical contrast of the two wafers demonstrates the thickness difference. **b**, Cross-sectional HAADF-STEM image showing a four-layer MoS_2 with 3R stacking. Scale bar, 2 nm. **c**, OM image showing the unidirectional 3R stacking of MoS_2 domains. Scale bar, 40 µm. 1L, one layer; 2L, two layers; 3L, three layers; 4L, four layers. **d**,**e**, False-colour diagram of MoS_2 with different layer numbers (**d**) and orientations (**e**) identified by AI corresponding to **c**. Scale bars, 40 µm. **f**, Statistics on the layer coverage via the AI model. **g**, Raman spectra of MoS_2 with different layer numbers transferred on SiO_2/Si. **h**, LEED pattern showing the 3R stacking of the as-grown MoS_2.

be ruled out because the bottom MoS_2 layer was continuous without exposed atomic steps. For surface nucleation, common nucleation centres include grain boundaries and point defects[35–38]. In our growth process, the first MoS_2 layer is single crystalline without grain boundaries. Therefore, it is reasonable to hypothesize that point defects in MoS_2 act as nucleation sites for 3R-MoS_2.

To obtain experimental evidence of defect-induced nucleation, we carried out a series of control experiments in which the first MoS_2 layer was exposed to ambient atmosphere or oxygen before the growth of the second layer (Methods). We found that after exposure, even using the same growth condition, we could not obtain phase-pure 3R-MoS_2 but instead a mixture of 2H and 3R stackings (Supplementary Fig. 10). The percentage of 3R domains decreased monotonically with the amount of exposure to ~50–60%, where there was little selectivity between 3R and 2H (Supplementary Fig. 11). Although oxygen, water and carbon can be physisorbed on the basal plane of MoS_2 (refs. 39,40, Supplementary Fig. 12 and Supplementary Table 1), the nucleation is not likely to occur at physically absorbed hydrocarbon species as they are removed under the growth conditions (Supplementary Fig. 13 and the 'Discussion about carbon absorption species on MoS_2' section in the Supplementary Information). Therefore, these control experiments point to the possible role of lattice defects in modulating the nucleation of the 3R and 2H phases.

To further substantiate our hypothesis, we performed DFT calculations to determine the nucleation energy of bilayer MoS_2 at common defect sites[41], including sulfur vacancies (V_S), double sulfur vacancies (V_{S2}), Mo_S and Mo vacancies (V_{Mo}) (Fig. 4a). These are the main defect types observed in our monolayer and bilayer MoS_2 (Supplementary Fig. 14). For each structure, we calculated the nucleation energy for 3R and 2H stackings and the energy difference ($E_{f\text{-}3R} - E_{f\text{-}2H}$) was used as a measure of selectivity. As shown in Fig. 4b, most defects have near-zero $E_{f\text{-}3R} - E_{f\text{-}2H}$, indicating no selectivity between 3R and 2H. The only defect favouring the nucleation of 3R over 2H is Mo_S anti-site with $E_{f\text{-}3R} - E_{f\text{-}2H} = -75$ meV per MoS_2. We further considered the passivation of Mo_S in ambient oxygen by calculating various passivated structures (Mo_S–O, Mo_S–O_2, Mo_S–OH, Mo_S–H and Mo_S–H_2O; Fig. 4a). The result shows that $E_{f\text{-}3R} - E_{f\text{-}2H}$ is significantly reduced by passivation, which explains the reduced 3R ratio in control experiments (Supplementary Figs. 10 and 11).

Further evidence of defect-promoted nucleation was obtained by the HAADF-STEM measurement of bilayer domains at the initial nucleation stage (Fig. 4c,d). Figure 4c,d shows the STEM image of a typical 3R bilayer domain with a diameter of ~7 nm, where a single, bright atomic defect is observed. Through experimental and simulated line profile analysis, we identify the defect site as Mo + Mo_S + S (Fig. 4e), suggesting that the defect is Mo_S in the first layer. For larger domains, we also observe Mo substitution sites near the centre (Supplementary Figs. 15 and 16). Therefore, we speculate that nucleation is most likely related to this defect type (more discussions are provided in the 'Discussion about the nucleation mechanism of 3R-MoS_2' section in the Supplementary Information). Moreover, Mo_S defects were observed at the centre of trilayer 3R domains (Supplementary Fig. 17). By contrast, no Mo_S

https://doi.org/10.1038/s41563-025-02274-y

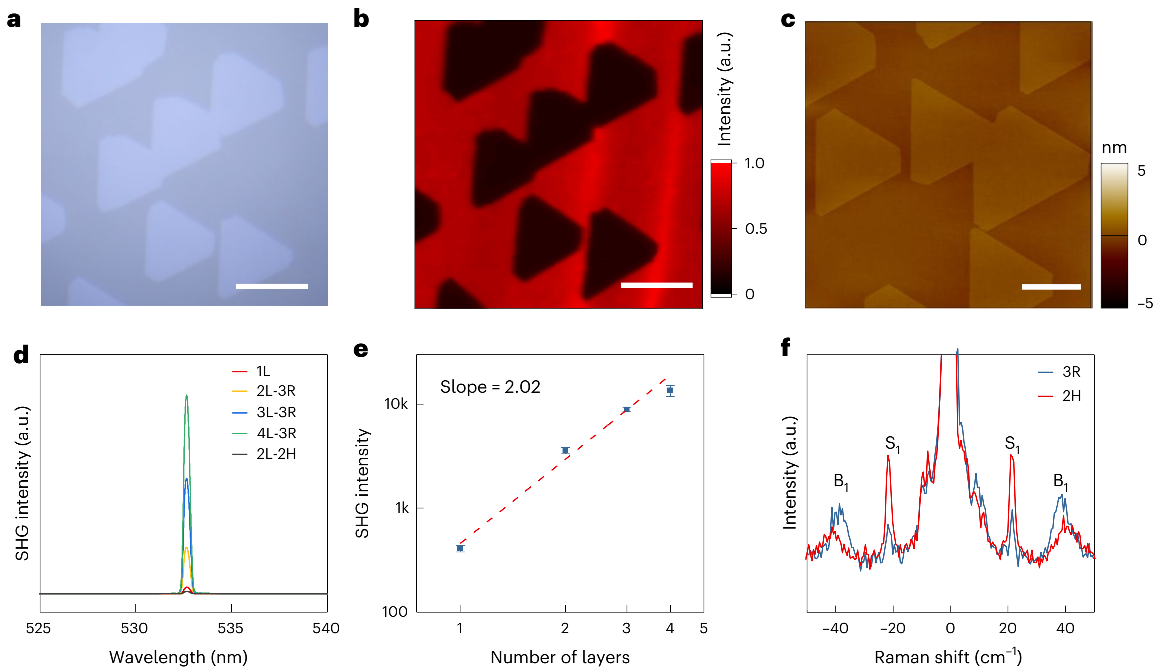

Fig. 2 | Spectroscopic characterizations of 3R-MoS$_2$. **a**, OM image of 3R-stacked bilayer MoS$_2$, which is composed of continuous monolayer and unidirectional, discrete bilayer domains. **b**, Corresponding PL mapping to **a**, showing the direct band emission of the monolayer zone and indirect band of the epitaxial bilayer domains. Scale bars, 10 µm (**a** and **b**). **c**, AFM height image demonstrating the high surface quality. Scale bar, 6 µm. **d**, Layer-number-dependent SHG spectra. **e**, Linear fitting of the SHG intensity with the layer number. Data are presented as mean values ± standard deviation. The statistical data are from ten samples. **f**, ULF Raman spectra of bilayer MoS$_2$ with 2H and 3R stacking.

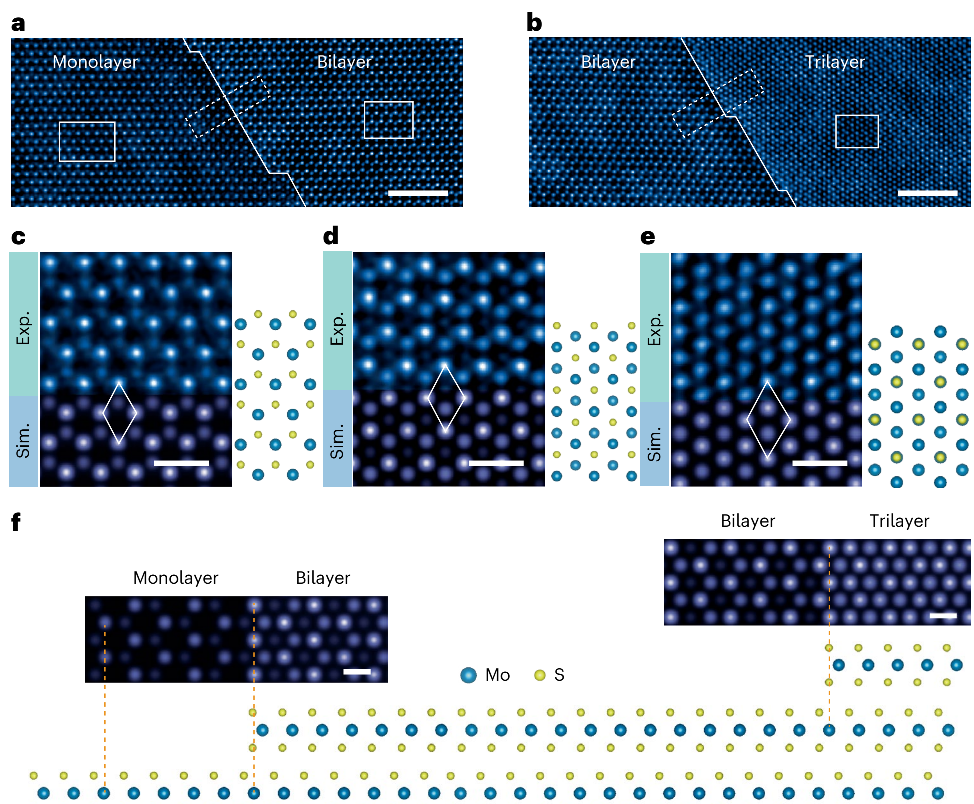

Fig. 3 | Atomic-resolved characterization of 3R-stacked MoS$_2$. **a**,**b**, Domain edge regions between mono-/bilayer R stackings (**a**) and bi-/trilayer stackings (**b**) with sharp edges. Scale bar, 2 nm. **c**–**e**, Experimental (Exp.) high-resolution HAADF-STEM images (left) and simulated (Sim.) images (right) of monolayer-stacked MoS$_2$ (**c**), bilayer-stacked MoS$_2$ (**d**) and trilayer-stacked MoS$_2$ (**e**). Experimental areas correspond to the regions marked with the white boxes in **a** and **b**. Scale bars, 0.5 nm. **f**, Simulated images of the interface between different layers and a schematic of the side view of the 3R configuration. Scale bars, 0.2 nm.

https://doi.org/10.1038/s41563-025-02274-y

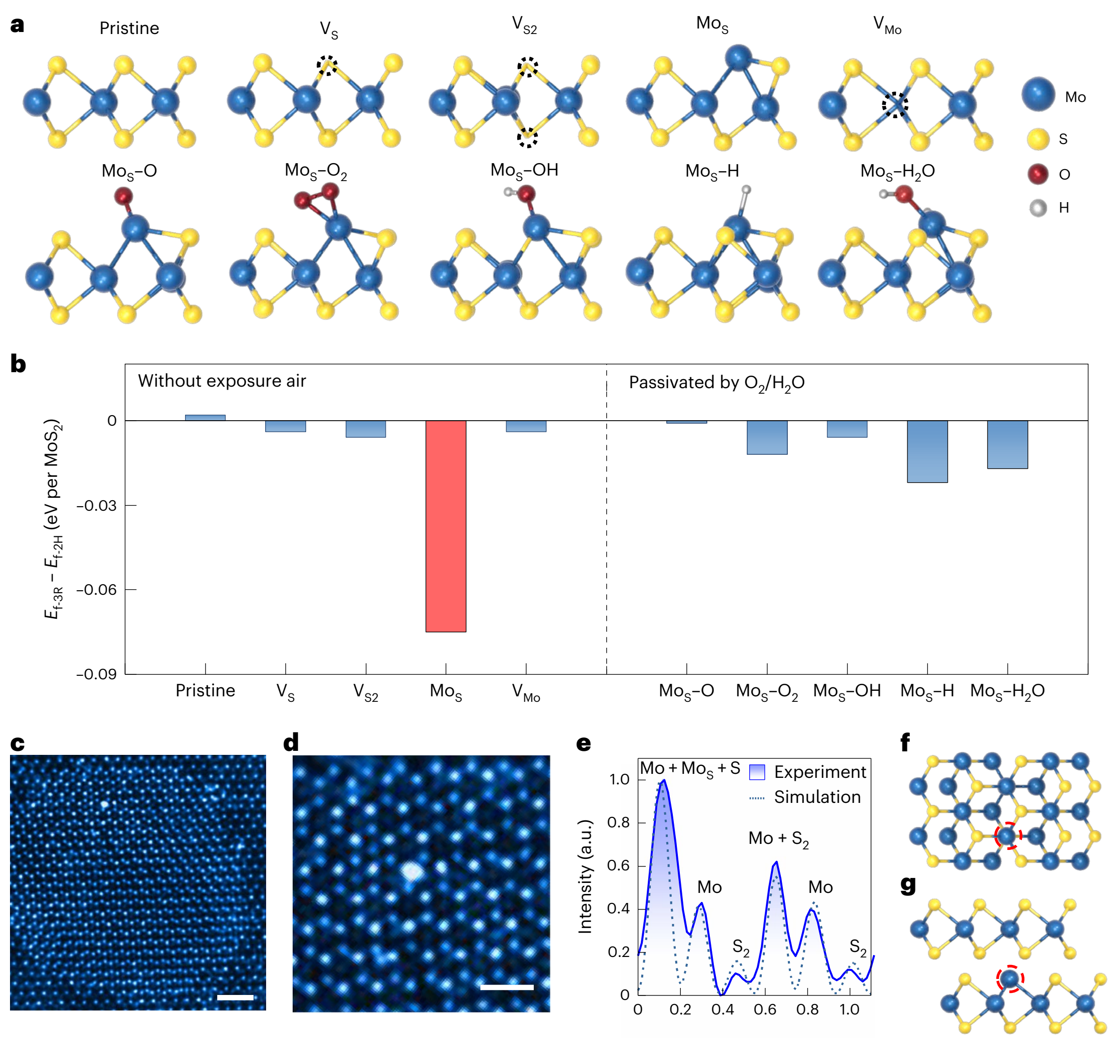

Fig. 4 | Mechanism of the selective growth of 3R-phase MoS_2. **a**, Atomic structures of pristine MoS_2 and defects, V_S, V_{S2}, Mo_S, V_{Mo} and Mo_S defects with absorption from oxygen and water when monolayer MoS_2 is exposed to ambient atmosphere. **b**, Formation energy difference between 3R and 2H stacking orders of bilayer MoS_2 with different defect types being presented on monolayer MoS_2. **c**, HAADF-STEM images of bilayer nucleation. **d**, A magnified image in **c**, which shows the MoS nucleation centre. The white dashed box in **c** corresponds to the regions where **d** resides. There is a brighter atomic site in the centre. **e**, Line profile analysis of the defect site along with the simulation results. **f**,**g**, Schematic of the top (**f**) and side (**g**) views of Mo_S defect-induced nucleation. Scale bars, 1 nm (**c**); 0.5 nm (**d** and **e**).

defects were found in the 2H domains (Supplementary Fig. 18). Other defect types beyond our calculations cannot be completely ruled out at this stage, which will be explored in future works.

Ferroelectricity and device applications of 3R-MoS_2

The broken inversion symmetry in 3R-MoS_2 gives rise to ferroelectricity. Prior works have demonstrated sliding ferroelectricity in mechanically exfoliated 3R-MoS_2 and twisted moiré structures[5–7], but CVD films have been rarely explored for device applications[20]. We first perform piezoresponse force microscopy (PFM) to verify the ferroelectricity in bilayer 3R-MoS_2 films at room temperature (Fig. 5a and Methods). Figure 5b,c shows the AFM height and the corresponding PFM phase images of a bilayer domain. Although the AFM shows uniform height across the bilayer region, the PFM phase shows two distinct colours, indicating ferroelectric domains with different polarization directions (more ferroelectric data are shown in Supplementary Fig. 19). The ferroelectric domains were revealed under tilted dark-field transmission electron microscopy (TEM; Supplementary Fig. 20)[8]. The sharp boundaries between the domains correspond to domain walls. The ferroelectric polarization switching is measured by an off-field piezoresponse loop in PFM (Fig. 5d). The amplitude and phase show typical butterfly and hysteresis loop features, respectively, with ±5-V coercive voltage and 180° phase shift. Different sample locations show very good reproducibility of ferroelectric switching (Supplementary Fig. 21). The out-of-plane piezoelectric coefficient d_{33} is measured to be ~0.31 pm V^{-1} for bilayer 3R-MoS_2 (Supplementary Fig. 22), in agreement with mechanically exfoliated samples[42].

As a ferroelectric semiconductor channel, 3R-MoS_2 can be used to build FeS-FETs with a non-volatile memory functionality. To demonstrate the unique advantage of large-area 3R-MoS_2 films, we fabricated device arrays using back-gate structures (Fig. 5e,f). Figure 5g plots the transfer characteristics of 48 FeS-FETs. The devices show a counter-clockwise hysteresis loop, a signature of ferroelectric memory. Due to the uniform 3R nature of the film, the devices exhibit good reproducibility with a narrow distribution of memory window (2.34 ± 0.46 V; Fig. 5h). By contrast, monolayer MoS_2 FETs fabricated using the same process show much more negligible clockwise hysteresis (Supplementary Fig. 23a), which is attributed to interface traps rather than ferroelectric switching.

https://doi.org/10.1038/s41563-025-02274-y

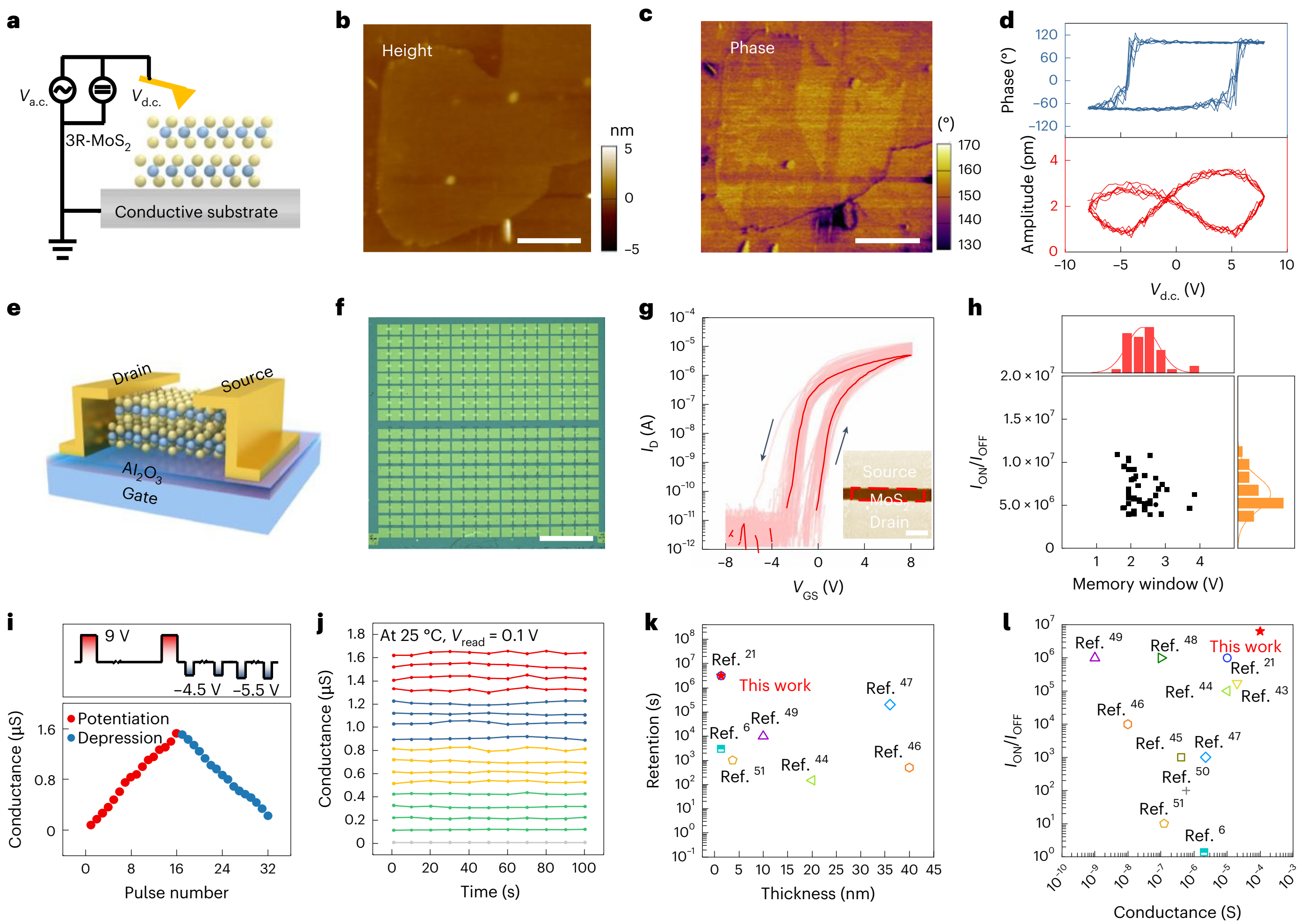

Fig. 5 | Ferroelectricity of R-stacked bilayer MoS_2. **a**, Schematic of vertical PFM measurements. **b**, AFM image of a bilayer flake on a monolayer film. Scale bar, 2 µm. **c**, Phase image of vertical PFM under $V_{a.c.}$ = 2 V corresponding to **b**. Scale bar, 2 µm. **d**, Amplitude and phase of the piezoresponse signal versus sample bias in vertical PFM. **e**, Schematic of a 3R-MoS_2 FeS-FET. **f**, OM image of an FeS-FET array. Scale bar, 300 µm. **g**, Transfer characteristics of the 3R-MoS_2 FeS-FET at sweep ranges of V_{GS} = ±8 V, showing an obvious counterclockwise hysteresis behaviour. The inset shows the AFM image of FeS-FET. Scale bar, 3 µm. **h**, Statistical distribution of the memory window and I_{ON}/I_{OFF}. **i**, Symmetric and linear multistate properties of the 3R-MoS_2 FeS-FET; the operation waveform are shown at the top of the figure. **j**, Multistate retention of 3R bilayer MoS_2 FeS-FET. **k**, Benchmark of the retention of FeS-FETs with different channel thicknesses. The Fes-FET in this work possesses a channel with the thinnest thickness but the highest retention. **l**, Benchmark of I_{ON}/I_{OFF} versus the conductance of FeS-FETs in the literature.

We further measure the retention characteristics of the FeS-FET (Supplementary Fig. 23b). The device is programmed to the ON/OFF state by ±10-V voltage pulses, followed by a d.c. sampling test for thousands of seconds. The decay of the resistive states is minimal within the test duration. By extrapolating the retention data, the ON/OFF ratio still exceeds three orders of magnitude after 10 years (Supplementary Fig. 23b). Moreover, the FeS-FET devices show good multibit characteristics. Figure 5i,j shows the potentiation and depression process of 16 storage states (4 bit) with good symmetry, linearity and retention, demonstrating the potential application of 3R-MoS_2 in analogue neuromorphic computing.

Finally, we benchmark our device performance with other 2D materials from the literature, including In_2Se_3, InSe, SnS and sliding 2D ferroelectric materials such as 3R-TMDs and twisted TMDs (Fig. 5k,l and Supplementary Table 2)[6,21,43–51]. Figure 5k plots the retention versus thickness. Our data are on the preferred top left corner with the best retention despite the smallest thickness of 1.3 nm. We should emphasize that all the other devices in the top left corner are based on exfoliated flakes rather than large-area CVD films. Figure 5l compares the ON-state conductance and ON/OFF ratio. Our device lies in the preferred top right corner with both high ON-state conductance and ON/OFF ratio. Overall, our FeS-FET devices exhibit one of the best ferroelectric device performances among 2D materials and offer a large-area device array. This makes the CVD 3R-MoS_2 very promising for device applications. We note that not all the FeS-FET devices exhibit ferroelectric memory behaviour, and the related discussions are provided in the 'Discussion about FeS-FET of 3R-MoS_2' section in the Supplementary Information.

Conclusion

In conclusion, we demonstrate the CVD growth of rhombohedral-stacked large-area MoS_2 films via homoepitaxy. A defect-promoted selective nucleation mechanism is proposed, which may inspire future research on growing artificially stacked 2D materials. The control of interlayer stacking by CVD offers a degree of freedom in the production of large-area 2D materials towards multifunctional integration.

Online content

Any methods, additional references, Nature Portfolio reporting summaries, source data, extended data, supplementary information, acknowledgements, peer review information; details of author contributions and competing interests; and statements of data and code availability are available at https://doi.org/10.1038/s41563-025-02274-y.

References

1. Wu, G. et al. Ferroelectric-defined reconfigurable homojunctions for in-memory sensing and computing. *Nat. Mater.* **22**, 1499–1506 (2023).
2. Liu, Y. et al. Promises and prospects of two-dimensional transistors. *Nature* **591**, 43–53 (2021).
3. Qiu, H. et al. Two-dimensional materials for future information technology: status and prospects. *Sci. China Inf. Sci.* **67**, 160400 (2024).
4. Wang, C., You, L., Cobden, D. & Wang, J. Towards two-dimensional van der Waals ferroelectrics. *Nat. Mater.* **22**, 542–552 (2023).
5. Wang, X. et al. Interfacial ferroelectricity in rhombohedral-stacked bilayer transition metal dichalcogenides. *Nat. Nanotechnol.* **17**, 367–371 (2022).
6. Weston, A. et al. Interfacial ferroelectricity in marginally twisted 2D semiconductors. *Nat. Nanotechnol.* **17**, 390–395 (2022).
7. Deb, S. et al. Cumulative polarization in conductive interfacial ferroelectrics. *Nature* **612**, 465–469 (2022).
8. Van Winkle, M. et al. Engineering interfacial polarization switching in van der Waals multilayers. *Nat. Nanotechnol.* **19**, 751–757 (2024).
9. Wang, L. et al. Correlated electronic phases in twisted bilayer transition metal dichalcogenides. *Nat. Mater.* **19**, 861–866 (2020).
10. Wu, F., Lovorn, T., Tutuc, E., Martin, I. & MacDonald, A. H. Topological insulators in twisted transition metal dichalcogenide homobilayers. *Phys. Rev. Lett.* **122**, 086402 (2019).
11. Suzuki, R. et al. Valley-dependent spin polarization in bulk MoS_2 with broken inversion symmetry. *Nat. Nanotechnol.* **9**, 611–617 (2014).
12. Scuri, G. et al. Electrically tunable valley dynamics in twisted WSe_2/WSe_2 bilayers. *Phys. Rev. Lett.* **124**, 217403 (2020).
13. Li, X. et al. Rhombohedral-stacked bilayer transition metal dichalcogenides for high-performance atomically thin CMOS devices. *Sci. Adv.* **9**, eade5706 (2023).
14. Rogée, L. et al. Ferroelectricity in untwisted heterobilayers of transition metal dichalcogenides. *Science* **376**, 973–978 (2022).
15. Shi, J. et al. 3R MoS_2 with broken inversion symmetry: a promising ultrathin nonlinear optical device. *Adv. Mater.* **29**, 1701486 (2017).
16. Dong, Y. et al. Giant bulk piezophotovoltaic effect in 3R-MoS_2. *Nat. Nanotechnol.* **18**, 36–41 (2023).
17. Yang, D. et al. Non-volatile electrical polarization switching via domain wall release in 3R-MoS_2 bilayer. *Nat. Commun.* **15**, 1389 (2024).
18. Suh, J. et al. Reconfiguring crystal and electronic structures of MoS_2 by substitutional doping. *Nat. Commun.* **9**, 199 (2019).
19. Liu, L. et al. Uniform nucleation and epitaxy of bilayer molybdenum disulfide on sapphire. *Nature* **605**, 69–75 (2022).
20. Wang, Q. et al. Layer-by-layer epitaxy of multi-layer MoS_2 wafers. *Natl Sci. Rev.* **9**, nwac077 (2022).
21. Yang, T. et al. Ferroelectric transistors based on shear-transformation-mediated rhombohedral-stacked molybdenum disulfide. *Nat. Electron.* **7**, 29–38 (2024).
22. Zhang, X. et al. Transition metal dichalcogenides bilayer single crystals by reverse-flow chemical vapor epitaxy. *Nat. Commun.* **10**, 598 (2019).
23. Deng, Y. et al. Controlled growth of 3R phase tantalum diselenide and its enhanced superconductivity. *J. Am. Chem. Soc.* **142**, 2948–2955 (2020).
24. Pan, Y. et al. Heteroepitaxy of semiconducting 2H-$MoTe_2$ thin films on arbitrary surfaces for large-scale heterogeneous integration. *Nat. Synth.* **1**, 701–708 (2022).
25. Chang, C. et al. Remote epitaxy of single-crystal rhombohedral WS_2 bilayers. *Nat. Commun.* **15**, 4130 (2024).
26. Qin, B. et al. Interfacial epitaxy of multilayer rhombohedral transition-metal dichalcogenide single crystals. *Science* **385**, 99–104 (2024).
27. Li, T. et al. Epitaxial growth of wafer-scale molybdenum disulfide semiconductor single crystals on sapphire. *Nat. Nanotechnol.* **16**, 1201–1207 (2021).
28. Puretzky, A. A. et al. Low-frequency Raman fingerprints of two-dimensional metal dichalcogenide layer stacking configurations. *ACS Nano* **9**, 6333–6342 (2015).
29. Liang, L. et al. Low-frequency shear and layer-breathing modes in Raman scattering of two-dimensional materials. *ACS Nano* **11**, 11777–11802 (2017).
30. Seol, M. et al. High-throughput growth of wafer-scale monolayer transition metal dichalcogenide via vertical Ostwald ripening. *Adv. Mater.* **32**, 2003542 (2020).
31. Strachan, J., Masters, A. F. & Maschmeyer, T. 3R-MoS_2 in review: history, status, and outlook. *ACS Appl. Energy Mater.* **4**, 7405–7418 (2021).
32. Wang, L. et al. Epitaxial growth of a 100-square-centimetre single-crystal hexagonal boron nitride monolayer on copper. *Nature* **570**, 91–95 (2019).
33. Chen, T. et al. Wafer-scale single-crystal hexagonal boron nitride monolayers on Cu (111). *Nature* **579**, 219–223 (2020).
34. Yang, P. et al. Epitaxial growth of centimeter-scale single-crystal MoS_2 monolayer on Au(111). *ACS Nano* **14**, 5036–5045 (2020).
35. Kang, K. et al. High-mobility three-atom-thick semiconducting films with wafer-scale homogeneity. *Nature* **520**, 656–660 (2015).
36. Zhang, X. et al. Defect-controlled nucleation and orientation of WSe_2 on hBN: a route to single-crystal epitaxial monolayers. *ACS Nano* **13**, 3341–3352 (2019).
37. Zhang, F. et al. Full orientation control of epitaxial MoS_2 on hBN assisted by substrate defects. *Phys. Rev. B* **99**, 155430 (2019).
38. Li, J. et al. General synthesis of two-dimensional van der Waals heterostructure arrays. *Nature* **579**, 368–374 (2020).
39. Addou, R. et al. Impurities and electronic property variations of natural MoS_2 crystal surfaces. *ACS Nano* **9**, 9124–9133 (2015).
40. Ferreira, F. et al. Adsorption of H_2, O_2, H_2O, OH and H on monolayer MoS_2. *J. Phys. Condens. Matter* **30**, 035003 (2018).
41. Hong, J. et al. Exploring atomic defects in molybdenum disulphide monolayers. *Nat. Commun.* **6**, 6293 (2015).
42. Konabe, S. & Yamamoto, T. Piezoelectric coefficients of bulk 3R transition metal dichalcogenides. *Jpn. J. Appl. Phys.* **56**, 098002 (2017).
43. Wang, J. et al. Logic and in-memory computing achieved in a single ferroelectric semiconductor transistor. *Sci. Bull.* **66**, 2288–2296 (2021).
44. Wang, L. et al. Exploring ferroelectric switching in α-In_2Se_3 for neuromorphic computing. *Adv. Funct. Mater.* **30**, 2004609 (2020).
45. Baek, S. et al. Ferroelectric field-effect-transistor integrated with ferroelectrics heterostructure. *Adv. Sci.* **9**, e2200566 (2022).
46. Wang, S. et al. Two-dimensional ferroelectric channel transistors integrating ultra-fast memory and neural computing. *Nat. Commun.* **12**, 53 (2021).
47. Xue, F. et al. Giant ferroelectric resistance switching controlled by a modulatory terminal for low-power neuromorphic in-memory computing. *Adv. Mater.* **33**, e2008709 (2021).
48. Singh, P. et al. Two-dimensional CIPS-InSe van der Waal heterostructure ferroelectric field effect transistor for nonvolatile memory applications. *ACS Nano* **16**, 5418–5426 (2022).
49. Liao, J. et al. Van der Waals ferroelectric semiconductor field effect transistor for in-memory computing. *ACS Nano* **17**, 6095–6102 (2023).

50. Bao, Y. et al. Gate-tunable in-plane ferroelectricity in few-layer SnS. *Nano Lett.* **19**, 5109–5117 (2019).
51. Kwon, K. C. et al. In-plane ferroelectric tin monosulfide and its application in a ferroelectric analog synaptic device. *ACS Nano* **14**, 7628–7638 (2020).

[1]National Laboratory of Solid State Microstructures, School of Electronic Science and Engineering and Collaborative Innovation Center of Advanced Microstructures, Nanjing University, Nanjing, China. [2]Suzhou Laboratory, Suzhou, China. [3]School of Integrated Circuits, Nanjing University, Suzhou, China. [4]Interdisciplinary Research Center for Future Intelligent Chips (Chip-X), Nanjing University, Suzhou, China. [5]School of Physics, Southeast University, Nanjing, China. [6]College of Engineering and Applied Sciences and Collaborative Innovation Center of Advanced Microstructures, Nanjing University, Nanjing, China. [7]Department of Materials, University of Oxford, Oxford, UK. [8]Key Laboratory of Mesoscopic Chemistry, School of Chemistry and Chemical Engineering, Nanjing University, Nanjing, China. [9]CAS Key Laboratory of Nano-Bio Interface & Key Laboratory of Nanodevices and Applications, i-Lab, Suzhou Institute of Nano-Tech and Nano-Bionics, Chinese Academy of Sciences, Suzhou, China. [10]Songshan Lake Materials Laboratory, Dongguan, China. [11]Jiangsu Key Laboratory of Micro and Nano Heat Fluid Flow Technology and Energy Application, School of Physical Science and Technology, Suzhou University of Science and Technology, Suzhou, China. [12]School of Integrated Circuit Science and Engineering, Nanjing University of Posts and Telecommunications, Nanjing, China. [13]These authors contributed equally: Lei Liu, Taotao Li, Xiaoshu Gong, Hengdi Wen. ✉e-mail: xrwang@nju.edu.cn

Methods

CVD growth of 3R-MoS_2

Single-side polished sapphire (0001) with a miscut angle of 1° towards the *a* axis ($c/a - 1°$) was used as the epitaxial substrate. Before growth, the substrates were subject to an annealing process at 1,000–1,100 °C for 4 h in air, which produces uniform bi-steps, as previously reported[19,27]. The growth was performed in a three-zone CVD system. Elemental sulfur (30 g, 99.995%) was utilized as the source and placed in a silica crucible and heated independently with an extra heating mantle at 180 °C and carried by 150 s.c.c.m. of Ar. Metallic Mo foils were used as the Mo sources and put in a separate tube from S. This structural design can avoid the contamination of Mo sources by S vapours. Most importantly, the Mo foils were oxidized in situ by 5–10 s.c.c.m. of O_2 to release MoO_3 vapours and carried by 50 s.c.c.m. of Ar into the growth chamber, which is a controllable way and ensures a stable, precise and continuous supply of sources. Since Mo metal has a very high melting temperature (2,620 °C), unoxidized Mo cannot evaporate at the heating temperature. When we switch on the O_2 flux, Mo can be oxidized into MoO_3, which can evaporate into the CVD system.

The growth comprises two steps. In the first step, a single-crystal monolayer film is epitaxially produced on the sapphire substrate at 950 °C. In the second step, the concentration of the Mo species was improved to boost the nucleation of the top layers by elevating the temperature of the Mo source from 600 °C to 800 °C and keep the growth temperature constant. According to our measurements, the MoO_3 vapour flux was increased from 5.8 μg min^{-1} (600 °C) to 110 μg min^{-1} (800 °C). The growth pressure is ~90 Pa and the whole growth process lasts about 30–60 min. The purity of the carrier gas sources is more than 99.999%. We note that O_2 mostly reacted with S vapour to form SO_2 during the growth, as measured by in situ mass spectrometry (Supplementary Fig. 25). The measured O_2 partial pressure of 0.495 Pa corresponded to chemical potential $\Delta\mu_O = -2$ eV. The formation energy of O_2 passivating Mo_S defects at $\Delta\mu_O = -2$ eV is much higher (by 3.42 eV) than in the air (Supplementary Fig. 26), indicating that Mo_S cannot be passivated by O_2 during growth.

The transfer of MoS_2 was done using the polymer-based transfer method. Poly(methyl methacrylate) (PMMA; Allresist 950K) was spin coated on MoS_2/sapphire at 2,000 rpm and baked at 150 °C. Then, a thermal release tape (TRT) was laminated and used to gently peel the PMMA/MoS_2 stack off the sapphire substrate in KOH water. The TRT/PMMA/MoS_2 stack was transferred onto the target substrate or a TEM grid and baked at 120 °C to release the TRT. Finally, the PMMA was removed by acetone.

Control experiments with the first MoS_2 layer exposed in ambient atmosphere or oxygen

After the monolayer MoS_2 growth was completed and cooled to room temperature, we kept it in the ambient atmosphere for 5 min, 3 h and 12 h. Then, the monolayer film was used as a template for the second-layer growth. For oxygen exposure, we introduced a mix of O_2 and Ar into the growth chamber after the single-crystal film cooled to room temperature. This mixture was maintained for 1 h with different O_2/Ar ratios to allow for O_2 adsorption under a total pressure of 1 bar. Afterwards, we pumped the chamber into a vacuum and proceeded with the next growth process.

Computation details

All the first-principles DFT calculations utilized the projector-augmented wave[52] potentials implemented in the Vienna ab initio simulation package[53]. The Perdew–Burke–Ernzerhof[54] generalized gradient approximation was used to treat the exchange–correlation functional. Grimme's DFT-D3 (ref. 55) scheme was used to characterize the van der Waals interaction, and the Brillouin zone was solely sampled at the gamma point. The structures underwent relaxation until the residual Hellman–Feynman force was <0.02 eV Å^{-1}, with an energy convergence criterion of 10^{-4} eV. A 400-eV energy cut-off was selected for the plane-wave basis sets. Additionally, to prevent interaction between adjacent images, a vacuum space of >10-Å thickness was included in the vertical direction. A $1 \times 2 \times 1$ *k*-point mesh was used for MoS_2 triangular clusters stacking on the first layer of MoS_2. The formation energy of 3R and 2H configurations for monolayer MoS_2 with a specific defect is calculated by $E_f = \frac{E_{total} - E_{2L\text{-}cluster} - E^{defect}_{1L\text{-}MoS_2}}{N_{2L\text{-}MoS_2}}$, where E_{total}, $E_{2L\text{-}cluster}$ and $E^{defect}_{1L-MoS_2}$ are the calculated energies of bilayer MoS_2 clusters stacking on monolayer MoS_2 with a specific defect, bilayer MoS_2 clusters and monolayer MoS_2 with a specific defect, respectively; and $N_{2L\text{-}MoS_2}$ is the number of MoS_2 units of bilayer MoS_2 clusters. In our calculations, the length of bilayer MoS_2 clusters is ~0.95 nm and $N_{2L-MoS_2} = 12$. Each supercell contains a single defect and different defect sites are considered when stacking the second layer.

The formation energies of Mo_S and Mo_S–O_2 defects are defined by

$$E_f = E_{defect} - E_{MoS_2} + \mu_S - \mu_{Mo/O}, \tag{1}$$

where E_{defect} and E_{MoS2} are the energies of MoS_2 with and without defects, respectively; μ_S and $\mu_{Mo/O}$ are the chemical potentials of S and added Mo/O, respectively.

The chemical potential of oxygen at the given partial pressure (P) and temperature (T) can be expressed as below.

$$\Delta\mu_{O(O_2)}(T,P) = \mu_{O(O_2)}(T,P) - \mu_{O(O_2)}(0,P^0)$$

$$= \frac{1}{2}\left(H^0_{O_2}(T) - TS^0_{O_2}(T) - H^0_{O_2}(0)\right) + \frac{1}{2}RT\ln\left[\frac{P_{O_2}}{P^0}\right] \tag{2}$$

According to the partial pressure of O_2 in the furnace during growth, the chemical potential of O is −2 eV, whereas $\Delta\mu_O = -0.296$ eV in the air at room temperature.

Optical characterizations

PL and Raman spectroscopy and mapping were performed by a custom-built system equipped with a 488-nm laser excitation and Princeton Instruments SP-2500 spectrometer. SHG spectroscopy and mapping were carried out in a customized system equipped with a piezo stage, an ultrafast 1,064-nm-wavelength laser (Rainbow 1064 OEM) and a photon-counting head (Hamamatsu Photonics H7421-50). A confocal micro-Raman spectrometer (Horiba LabRAM HR Evolution) with an 1,800-lines-per-mm grating was used to test the ULF Raman data.

PFM measurements

All the PFM measurements were adapted to the Dart-SS-PFM mode. The vertical PFM mapping, hysteresis loop and KPFM measurements were performed on the bilayer 3R-MoS_2 that was transferred onto the Pt substrate by PMMA. PFM measurements were conducted with Asylum Research Cypher S AFM device at room temperature. We used Asyelec-01-R2 with a force constant of around 2.8 N m^{-1} and a contact resonance frequency of around 280 kHz with the applied a.c. bias voltage of 2 V for the Dart-SS-PFM measurements.

Vertical PFM (VPFM) captures the vertical signal of the cantilever. In real VPFM measurements, the recorded VPFM signal is fairly complex, arising from the interplay among piezoelectricity, electrostatic interaction[56], electrochemical strain[57] and even the experimental setup[58]. All those mechanisms may contribute as a background VPFM signal to distort a relatively small VPFM response of the sample. To obtain the pure electromechanical response of 3R-MoS_2, we use vector decomposition to remove the background signal. A mask can be manually sketched based on phase and amplitude maps to distinguish the 3R-MoS_2 area and monolayer MoS_2 (background) area. The background VPFM signal of one scan line ($\bar{A}e^{i\bar{\theta}}$) is calculated by the mean measured VPFM vector of monolayer MoS_2 area ($A_m e^{i\theta_m}$):

https://doi.org/10.1038/s41563-025-02274-y

$$\bar{A}e^{i\bar{\theta}} = \frac{1}{n}\sum_{j=1}^{n} A_{m,j}e^{i\theta_{m,j}}; \quad (3)$$

the decoupled VPFM vector for every pixel ($A_d e^{i\theta_d}$) is determined by subtracting this background VPFM vector from the measured VPFM vector ($A_m e^{i\theta_m}$):

$$A_d e^{i\theta_d} = A_m e^{i\theta_m} - \bar{A}e^{i\bar{\theta}}, \quad (4)$$

and the corresponding decoupled phase (θ_d) and amplitude (A_d) maps are shown in Supplementary Fig. 22.

TEM characterization

Epitaxial 3R-MoS_2 was transferred onto a TEM grid (Cu grid with a carbon array microgrid). The atomic-resolved HAADF-STEM and cross-sectional HAADF-STEM of different layers were captured on FEI Themis Z at an accelerating voltage of 300 kV. The in-plane HAADF-STEM images were filtered by Gaussian filters. The tilt dark-field TEM images were captured on an aberration-corrected STEM Titan Cubed G2 60-300 system with an accelerating voltage of 60 kV. All the in-plane STEM simulations used scripts based on the modified MULTEM package using MATLAB R2020b and accelerated by GPU calculations[59]. The STEM image simulations are run at 300 kV with an aberration-free probe and a convergence angle of 22.5 mrad. The scanning pixel size is 0.1 Å. STEM detector angle is set to 75–200 mrad, which is consistent with the experiment condition. The source size and nonlinear effect of the detector are considered in the simulation.

Device fabrication and measurement

Here 20-nm Al_2O_3 was deposited by plasma-enhanced atomic layer deposition as a dielectric insulator at 150 °C using O_2 plasma as the oxygen source and trimethyl aluminium as the precursors on a heavily doped silicon substrate as the global gate. After that, bilayer MoS_2 was transferred onto it by using TRT. Then, electron-beam lithography and reactive ion etching with O_2 plasma were used to pattern the MoS_2 nanoribbons. The contact electrodes were defined by electron-beam lithography, and 15 nm of Sb and 30 nm of Au were finally deposited as the source and drain, to suppress Fermi-level pinning and reduce the contact resistance[60]. Electrical measurements were performed at room temperature using a Keithley 4200 semiconductor characterization system with four source meter units for the d.c. test and 4,225 remote pulse and switch modules for the pulse test under a base pressure of 10^{-6} torr in the Lakeshore CRX-VF probe station. With source meter units, the transfer and output properties were characterized. The MoS_2 FET was programmed to the ON state (or erased to the OFF state) with 10 V/2 s (or −10 V/2 s); then, a d.c. sampling test proceeded for thousands of seconds, thereby extrapolated to 10 years of retention by linear fitting. As for the multistate test, the potentiation (or depression) process was realized by identical 9 V/40 ms (or −4.5 V/5 ms for the first eight states and −5.5 V/5 ms for the second eight states) generated by 4,225 remote pulse and switch modules at the gate, whereas the drain and source of the FET were both grounded. Different pulse conditions in depression progress were applied for linear weight update[61]. Afterwards, the typical output curves were obtained under a small V_{DS} (±0.2 V) range to read the conductance of MoS_2 FET.

AI recognition of MoS_2 layer numbers

Recognizing the limitations posed by the background tilt, which affects the direct use of brightness pixel counts for layer determination, we use a machine-learning-based approach enhanced by a comprehensive calibration process for determining the layer numbers of 2D materials viewed using OM. This process adjusts for variations in lighting conditions, ensuring accurate feature extraction critical for layer identification. Our calibration procedure extends beyond the traditional focus on image corners to include the edges and the centre, capturing a comprehensive range of brightness levels across the image. This thorough calibration ensures that the adjustments made for lighting conditions are uniformly applied, thereby rectifying the illumination inconsistencies inherent in the OM of 2D materials. Following calibration, the process proceeds with the extraction of features critical to our analysis, including the pixel coordinates (X, Y) and RGB values. These extracted features serve as inputs to our machine learning model, facilitating accurate predictions of layer numbers across the sample.

In the selection of an appropriate machine learning model, we leverage an automated machine learning function to evaluate various algorithms, ultimately selecting a support vector machine model for its superior performance and captivity at handling nonlinear relationships and complex patterns present in our MoS_2 OM images (Supplementary Fig. 4a). This model is trained on a labelled dataset, where each pixel is associated with a known layer number, ensuring a robust framework capable of generalizing from our training data to accurately predict layer numbers in new, unseen images. Utilizing the trained support vector machine model, we predict the layer number for each pixel in the image, allowing for a detailed mapping of layer distribution across the sample. This approach enables the precise identification of different material layers, offering a granular view of the sample's composition.

A detailed map displaying each layer's distribution, colour coded for clarity and ease of interpretation. The model's confusion matrix highlights the accuracy and precision in predicting various layer numbers, thereby providing an insight into the model's effectiveness (Supplementary Fig. 4b). Distribution histograms quantify the percentage coverage of each layer within the samples, alongside cumulative histograms that offer a nuanced understanding of overall layer distribution.

Our analytical approach not only underscores the efficacy of combining image calibration, feature extraction and machine learning in accurately determining the layer numbers but also facilitates a deeper understanding of the 2D materials examined. By leveraging comprehensive calibration alongside a sophisticated support vector machine model selected through automated machine learning, our methodology represents a significant advancement over traditional analysis techniques, offering enhanced accuracy and insight into the material properties.

MoS_2-domain orientation analysis and image segmentation model

To accurately and efficiently distinguish the orientation of MoS_2 crystals and apply pseudocolor processing to crystals with different orientations, an image segmentation model based on deep learning is considered. The principle of image segmentation involves dividing the image into several subregions that share similar colour or texture characteristics, which correspond to different objects or different parts of objects. These subregions, constituting the complete subset of the image, are mutually exclusive. Traditional segmentation methods are represented by graph-cut, whereas deep learning models include U-Net, FCN and DeepLab[62]. In this paper, the U-Net model for image segmentation is applied, and the principle of this model and its segmentation results are introduced below.

The U-Net network is composed of two parts: the first half is dedicated to feature extraction (with MobileNet as the base model), and the second half involves upsampling. This structure is also referred to as an encoder–decoder architecture in some studies. The overall structure of this network resembles the uppercase letter 'U', which is the reason behind its name, U-Net. A diagram of its structure is presented in Supplementary Fig. 4c.

The overall structure of U-Net can be divided into two parts: an encoder and a decoder (Supplementary Fig. 4d). The encoder is responsible for progressively extracting features from the input image, reducing the image resolution, whereas the decoder gradually restores the resolution and generates the final segmentation result.

The encoder part of U-Net consists of multiple downsampling layers, each comprising a convolutional layer followed by a pooling layer, which is used to progressively reduce the image size and extract features. This approach is aimed at incorporating context information at different scales. The downsampling section can be considered a conventional convolutional neural network where features are gradually reduced, and spatial information is discarded. This section is composed of two convolution operations and two max-pooling operations, with a rectified linear unit activation function following each convolutional operation. After each max-pooling operation, the width and height of the feature map are halved.

The decoder part of U-Net includes multiple upsampling layers and corresponding skip connections. Upsampling layers are used to gradually increase the image size, whereas skip connections are used to link the feature maps from the encoder to the corresponding feature maps in the decoder, preserving more spatial details and semantic information. Each upsampling layer also has a corresponding convolutional layer for further feature processing. The upsampling section gradually restores the features to their original size and reintegrates lost spatial information back into the features. This section consists of an upsampling operation and a convolution operation, with each convolution operation followed by a rectified linear unit activation function, too.

Within these two parts, numerous skip connections link features from the downsampling section to the upsampling section, allowing for the segmentation to utilize both coarse and fine features. These skip connections enable U-Net to better preserve spatial information, thereby enhancing the accuracy of segmentation.

The loss function of U-Net: U-Net is utilized for image segmentation, where our objective is to assign each pixel in the input image to its respective category. We can use cross-entropy as the loss function, which is defined as follows[63]:

$$\mathrm{Loss} = -\frac{1}{N}\sum_{i=1}^{N}\sum_{j=1}^{C} y_{ij}\,\log[p_{ij}],$$

where N denotes the number of samples, C represents the number of categories, y_{ij} is the true label indicating whether the ith sample belongs to the jth category, and p_{ij} is the probability output by the network that the ith sample belongs to the jth category. Furthermore, during training, it is necessary to use the backpropagation algorithm to calculate gradients and update the network parameters.

For an AFM image, the encoder of the convolutional neural network, U-Net, is first used to extract the features, obtaining high-level semantic feature maps; then, the decoder restores the feature map to its original size. During the training phase, a loss function is constructed using the model's predicted map and the sample's true label map, thereby facilitating model training. In the inference phase, the model's predicted map serves as the final output. A distinctive feature of U-Net, setting it apart from other common segmentation networks, is its unique feature fusion method—concatenation. U-Net uses concatenation to combine features along the channel dimension, forming denser features[64].

In U-Net, the pooling layer enables multiscale feature recognition of the image by the network. The upsampling section integrates outputs from the feature extraction segment, effectively fusing multiscale features. For example, the features of the last upsampling originate both from the output of the first convolutional block (same-scale features) and from the output of the upsampling (larger-scale features). Such connections, which occur throughout the network, result in up to four instances of fusion. The modified segment model is able to judge the MoS_2 crystal orientation within 0.1 s, reaching an accuracy of >98%.

Data availability

All data are available in the article and its Supplementary Information. Source data are provided with this paper.

References

52. Blöchl, P. E. Projector augmented-wave method. *Phys. Rev. B* **50**, 17953–17979 (1994).
53. Kresse, G. & Furthmüller, J. Efficient iterative schemes for ab initio total-energy calculations using a plane-wave basis set. *Phys. Rev. B* **54**, 11169–11186 (1996).
54. Perdew, J. P., Burke, K. & Ernzerhof, M. Generalized gradient approximation made simple. *Phy. Rev. Lett.* **77**, 3865–3868 (1996).
55. Grimme, S., Antony, J., Ehrlich, S. & Krieg, H. A consistent and accurate ab initio parametrization of density functional dispersion correction (DFT-D) for the 94 elements H-Pu. *J. Chem. Phys.* **132**, 154104 (2010).
56. Ming, W., Huang, B. & Li, J. Decoupling competing electromechanical mechanisms in dynamic atomic force microscopy. *J. Mech. Phys. Solids* **159**, 104758 (2022).
57. Chen, Q. N., Ou, Y., Ma, F. & Li, J. Mechanisms of electromechanical coupling in strain based scanning probe microscopy. *Appl. Phys. Lett.* **104**, 242907 (2014).
58. Jungk, T., Hoffmann, Á. & Soergel, E. Quantitative analysis of ferroelectric domain imaging with piezoresponse force microscopy. *Appl. Phys. Lett.* **89**, 163507 (2006).
59. Lobato, I. & Van Dyck, D. MULTEM: a new multislice program to perform accurate and fast electron diffraction and imaging simulations using graphics processing units with CUDA. *Ultramicroscopy* **156**, 9–17 (2015).
60. Li, W. et al. Approaching the quantum limit in two-dimensional semiconductor contacts. *Nature* **613**, 274–279 (2023).
61. Jerry, M. et al. Ferroelectric FET analog synapse for acceleration of deep neural network training. In *IEEE International Electron Devices Meeting (IEDM)* 6.2.1–6.2.4 (IEEE, 2017).
62. Beeche, C. et al. Super U-Net: a modularized generalizable architecture. *Pattern Recognit.* **128**, 108669 (2022).
63. Zhao, P. et al. A new method for classifying and segmenting material microstructure based on machine learning. *Mater. Des.* **227**, 111775 (2023).
64. Bangaru, S. S., Wang, C., Zhou, X. & Hassan, M. Scanning electron microscopy (SEM) image segmentation for microstructure analysis of concrete using U-net convolutional neural network. *Autom. Constr.* **14**, 104602 (2022).

Acknowledgements

This work was supported by the National Key R&D Program of China (grant nos. 2022YFB4400100, 2023ZD0120704, 2023YFF1500500 and 2021YFA0715600); the National Natural Science Foundation of China (grant nos. T2221003, 62322408, 62204124, 62204113, U24A20295, 22222302, 32301156 and 61927808); the Natural Science Foundation of Jiangsu Province (grant nos. BK20220773, BK20232024 and BK20222007); the Key Laboratory of Advanced Photonic and Electronic Materials, Collaborative Innovation Center of Solid-State Lighting and Energy-Saving Electronics, the Big Data Computing Center of SEU and National Supercomputing Center in Tianjin. We would like to express our sincere gratitude to the Interdisciplinary Research Center for Future Intelligent Chips (Chip-X) and the Yachen Foundation for their invaluable support. We also thank R. Zhu and C. Liu at Oxford Instruments for their help in the ferroelectric characterization. X.W. acknowledges support from the New Cornerstone Science Foundation through the XPLORER PRIZE.

Author contributions

X.W. conceived and supervised the project. L.L. performed the CVD growth under the supervision of T.L., with assistance from S.Z. and X.Z. X.G., L.M. and J.W. performed the DFT calculations. M.F., H.Z. and

https://doi.org/10.1038/s41563-025-02274-y

N.Z. performed the AI identification of layer thickness and 3R ratios. L.Z., X.H., S.W. and K.Z. performed the TEM characterization and data analysis. Z.D. performed the STEM simulation. L.L., F.Z. and Z.H. performed the PL, Raman and SHG tests and sample transfer. S.F. and W.X. performed the ULF Raman test. Y.L., G.L., L.T. and Y.J. contributed to the ferroelectric characterization and data analysis. H.W. and Z.Y. fabricated and tested the MoS_2 FeS-FETs. L.L., T.L., L.M., J.W. and X.W. co-wrote the paper with input from the other authors. All authors contributed to the discussions.

Competing interests

The authors declare no competing interests.

Additional information

Supplementary information The online version contains supplementary material available at https://doi.org/10.1038/s41563-025-02274-y.

Correspondence and requests for materials should be addressed to Xinran Wang.

Peer review information *Nature Materials* thanks the anonymous reviewers for their contribution to the peer review of this work.